Tailoring the surface of perovskite through in-situ growth of Ru/RuO₂ nanoparticles as robust symmetrical electrodes for reversible solid oxide cells

Junkai Wang[a], Jun Zhou[a, *], Jiaming Yang[a], Dragos Neagu[b], Lei Fu[a], Zhongjie Lian[a], Tae-Ho Shin[c], Kai Wu[a]

[a] State Key Laboratory of Electrical Insulation and Power Equipment, Xi'an Jiaotong University, Xi'an 710049, People's Republic of China

[b] Department of Chemical and Process Engineering, University of Strathclyde, 16 Richmond Street, Glasgow, G11XQ, UK.

[c] Energy Materials Center, Korea Institute of Ceramic Engineering & Technology, (52851) 101, Soho-ro, Jinju-si, Gyeongsangnam-do, South of Korea.

Abstract：

Although numerous perovskite oxides can enhance the electrochemical activity via exsolved metallic nanoparticles, most of them can only be applied as catalysts in a reduced atmosphere. These nanoparticles will cause serious performance degradation in oxidizing conditions due to the formation of low-conductive metal oxides. This poses a big challenge to the design of highly active catalysts of electrochemical devices. Herein, a unique and simple method is demonstrated for the synthesis of Ru/RuO$_2$ nanoparticles via *in-situ* growth on the surface of perovskite oxide. The electrode material $(La_{0.75}Sr_{0.25})_{0.9}Cr_{0.5}Mn_{0.45}Ru_{0.05}O_{3-\delta}$ (LSCMR) was designed through careful choice of composition and the core idea is to make use of the exsolved nanoparticles concept applied for the first time at both hydrogen electrode and oxygen electrode for symmetrical solid oxide cells. Inspired by exsolved Ru and RuO$_2$, the surface-decorated LSCMR exhibit significantly enhanced electrochemical activity for both H$_2$ and O$_2$ respectively, accompanied by high redox long-term stability. Moreover, simple,

low-cost, and environmental-friendly synthesis of Ru/RuO$_2$ nanoparticles on the substrate of typical perovskites is realized with this *in-situ* growth approach.

∗Corresponding author.

E-mail: zhoujun@mail.xjtu.edu.cn

1. Introduction

The energy interconnection is considered to be one of the solutions to solve energy crisis in the future. [1] Therefore, there is a need to develop high efficiency and reversible energy conversion methods between various energy resources, such as electricity and chemical energies. Reversible solid oxide cells (RSOCs) have been attracting great attention due to their multiple functionalities and high potential efficiency, such as generating electricity as fuel cells (FC mode) and producing hydrogen as electrolysis cells (EC mode).[2] Generally, the traditional RSOCs consist of three different components, both fuel electrode and oxygen electrode, separated by a dense electrolyte.[3] Usually, the electrodes consist of different materials, in order to efficiently carry out the fuel oxidation reaction (FOR), oxygen reduction reaction (ORR), hydrogen evolution reaction (HER), and oxygen evolution reaction (OER), respectively.[4] However, the range of necessary materials to provide these functions poses limitations on material selection, and increases the complexity of manufacturing, operation and maintenance, thus limiting applicability. Additionally, the long-term stability of RSOCs operated under high temperatures is still a challenge.[5] Especially, the interface between electrode and electrolyte is subjected to different conditions if the operation mode switched between FC and EC.[6]

One approach used to overcome some of the above limitations is to fabricate RSOCs using the same electrode material for both fuel electrode and oxygen electrode, in so-called symmetric solid oxide cells (SSOCs).[7] Such devices would exhibit obvious advantages over current designs, including but not limited to lower cost, simpler fabrication process and minimizing interfacial problems among different cell components,

possibly improving device lifetime and thus requiring lower maintenance. Considering that the fuel and oxygen electrodes operate in highly reducing and oxidizing environments, respectively, for reversible SSOCs it is important to seek out suitable materials fulfilling the requirements applicable to both types of atmospheres.[8] This includes high electronic and ionic conductivity, high electrochemical catalytic activity and durability in both oxidizing and reducing conditions. [15] To date, several redox-stable perovskite-type oxides have been considered for this role[7b, 8-9]. However, most of these have not been applied as both fuel and oxygen electrodes simultaneously for reversible SSOCs, and the catalytic activity of these electrodes is still far from the requirements.

In order to enhance the electrochemical cell performance, one of the most common methods is to enhance surface reactivity by functionalizing the surface with nanosized catalysts, such as Pt, Pd, Ru, Ni for fuel electrode and Pt, Ag for oxygen electrode, respectively.[10] Traditionally, this has been carried out through the infiltration method, which has been developed and widely used to fabricate surface-modified fuel electrodes for both solid oxide fuel cell (SOFC) and solid oxide electrolysis cell (SOEC).[11] However, for this process, complicated deposition steps and expensive precursors are generally needed to control the morphology of the nanosized catalysts. Although this approach leads to considerable cell performance increase in SOFC and SOEC separately, it is difficult to obtain and maintain uniform particle size and distribution of the nanosized catalysts, on the fuel electrode and oxygen electrode backbone simultaneously. Recently, an alternative approach called in-situ growth of metal nanoparticles from perovskite oxides has been proposed to be a more effective, single-step, and low-cost method to

prepare the catalysts-modified electrodes.[12] As compared to infiltration methods, particles produced by exsolution are also partly embedded in the support (socketed) which greatly enhances their durability, helping to maintain uniform particle size and distribution during long-term operation. So far, perovskite oxides have been generally demonstrated to be capable of growing metal nanoparticles in situ under reducing condition, that is, at the fuel electrodes. This method has generally not been applied at the oxygen electrode because most metal nanoparticles will form metal oxides under such conditions at high temperatures, which usually leads to poor electrochemical activity for both ORR and OER.

In this work, in order to obtain high, long-lasting electrochemical performance together with good redox stability between different modes (EC and FC), we develop a new redox-stable, a symmetric electrode with A-site deficient perovskite $(La_{0.75}Sr_{0.25})_{0.9}Cr_{0.5}Mn_{0.5-x}Ru_xO_{3-\delta}$ (x=0-0.05) as host ceramic electrode material. We demonstrate that this host ceramic can generate uniformly distributed Ru metallic nanoparticles at the surface, through in situ exsolution after reduction. Furthermore, when the system is then exposed to conditions encountered at the oxygen electrode, core-shell structured Ru/RuO_2 nanoparticles were formed. This endows the material with high electrochemical activity towards both oxygen reduction and hydrogen oxidation.

2. Results and discussion

Recent reports suggest that the exsolution from perovskites is driven by lattice reduction and controlled by bulk and surface defects and external conditions.[2d, 11c] A deficiency of the A-site ion in ABO_3 is one of the key factors to control the ease and the quality of

exsolution, as well as enhancing electronic and ionic conductivity. Thus, The designed

A-site deficient $(La_{0.75}Sr_{0.25})_{0.9}Cr_{0.5}Mn_{0.5}O_{3-\delta}$ (LSCMRu$_{A-0}$),

$(La_{0.75}Sr_{0.25})_{0.9}Cr_{0.5}Mn_{0.475}Ru_{0.025}O_{3-\delta}$ (LSCMRu$_{A-25}$), $(La_{0.75}Sr_{0.25})_{0.9}Cr_{0.5}Mn_{0.45}Ru_{0.05}O_{3-\delta}$

(LSCMRu$_{A-5}$) powders were prepared by solid-state reaction in air, following a reduction

process with the calcined treatment in 5% H_2/N_2 at different temperatures, respectively.

XRD analysis confirms that the as-prepared LSCMRu$_{A-5}$ oxides exhibit a structure with

space group *R-3c* (167) at room temperature (Supporting Information, Figure S1 and

Table S1). On reduction, the perovskite-type structure is preserved for all samples and a

unit cell expansion is observed due to the reductions of B-site elements (Cr, Mn, and Ru)

from higher oxidation states to lower oxidation states.

Generally, the structure of ABO_3 perovskite can be complex due to the tilting of the

oxygen octahedra and/or the ordering of both A-site and B-site elements. Additionally, this

can undergo further structural transformations depending on temperature and

atmosphere.[13] Such changes are important to study and understand since they affect

interaction with adjacent cell components and interfaces which is important for both cell

manufacture and operation. For example, a phase transition is observed in the

unsubstituted $La_{0.75}Sr_{0.25}Cr_{0.5}Mn_{0.5}O_3$, from *R-3c* to *Pm-3m* space group over the

temperature from 500 to 1100 °C, in an ambient atmosphere.[14] To investigate phase

evolution of both as-prepared and reduced LSCMRu$_{A-5}$ at high temperature, in situ

high-temperature X-ray diffraction (HT-XRD) studies have been carried out in air up to

temperatures of 1000 °C (**Figure 1,** Table S3). The results indicate that LSCMRu$_{A-5}$ also

underwent a reversible second-order phase transition in a thermal-cooling cycle under air.

The fraction of the *Pm-3m* space group increases with increasing temperature up to 1000 °C and then the *R-3c* space group becomes the dominant again at lower temperatures. Similar behavior was observed in as-prepared LSCMRu$_{A-0}$ and reduced LSCMRu$_{A-5}$, respectively (Supporting Information, Figure S2 and S3, Table S2 and S4). This vividly depicts that the phase transition in LSCMRu$_{A-5}$ is not an abrupt step but a gradual process. The second-order phase transition of LSCMRu$_{A-5}$ is favorable for SOC fabrication and operation to prevent the delamination of the electrode and electrolyte.[14-15] Moreover, the phase transition is reversible for both as-prepared and reduced LSCMRu$_{A-5}$ compounds, minimizing the stress to which the electrodes are subjected to during redox cycling in different operating modes, such as SOFC and SOEC.

High-resolution transmission electron microscopy (HRTEM) was used to characterize the nanostructure of the LSCMRu$_{A-5}$ powders, as shown in **Figure 2**. Compared to the reduced LSCMRu$_{A-0}$ (Supporting Information, Figure S4), numerous nanosized particles were exsolved in a uniform distribution, on the surface of the reduced LSCMRu$_{A-5}$ (**Figure 2a**). The average diameter of nanoparticles is around 4-8 nm. **Figure 2b** shows a single crystal with visible lattice fringes at a spacing of 0.132 nm of the (110) plane for the Ru (PDF no. 06-0663). Scanning transmission electron microscopy (STEM) along with energy-dispersive X-ray spectroscopy (EDS) analysis confirmed the exsolution of Ru nanoparticles. **Figure 2c** shows STEM-EDS image and an overall elemental mapping of reduced LSCMRu$_{A-5}$, including an exsolved Ru nanoparticle at the surface. And the population of exsolved Ru nanoparticles of LSCMRu$_{A-5}$ is around 1486 particles um^{-2}. After oxidized in air, the population of nanoparticles decreased to 1113 particles um^{-2}

(Supporting Information, Figure S5).

HRTEM images also indicated that core/shell structured Ru/RuO_2 nanoparticles formed on the surface of LSCMRu$_{A-5}$ after calcination at 800 $^{\circ}$C in air for 3 h, with a thickness of RuO_2 shell of around 2-3 nm. The interface between the Ru core and RuO_2 shell is highlighted in **Figure 3a**. However, upon reduction at 750 $^{\circ}$C in 5% H_2/95% N_2 for 10 h, the RuO_2 shell was reverted to highly crystalline, metallic Ru, as confirmed by STEM-EDS mapping images (**Figure 3b**). This phenomenon depicts a reversible transformation between Ru and RuO_2 only by changing the atmospheres (**Figure 3c and 3d**), which is consistent with previous literature.[16] However, as compared to previous reports here, we demonstrate how this process can be achieved seamlessly and *in-situ*, thus preparing Ru/RuO_2 nanostructures on a perovskite substrate for noble metal catalysts. The fitted ex-situ XPS curves of Ru were used to quantify the proportion of Ru in various valence states (Ru^0, Ru^{3+}, and Ru^{4+}) in LSCMRu$_{A-5}$, as showed in **Figure 3e**. After reduced, the content of Ru^{3+} in LSCMRu$_{A-5}$ increased from 37% up to 68%, while the content of Ru^{4+} decreased from 63% down to 15% (Supporting Information, Figure S6, Table S5 and Table S6). The amount of exolved Ru was also predicted by approximately 16% in reduced LSCMRu$_{A-5}$. Moreover, the mole ratio of total Ru^{4+} increased to 60%. Among these, 28% Ru^{3+} was oxidized to Ru^{4+} after the reduced LSCMRu$_{A-5}$ powders was calcined in air at 750 $^{\circ}$C for 2 h. Thus, the additional 15% Ru^{4+} are from the metallic Ru due to the RuO_2 shell was formed after oxidation. Moreover, the peak of Raman spectra near 645 cm^{-1} decreases in intensity after reducing, indicating that the oxygen bridge bonds related to Ru could be broken and the Ru element exsolved from the lattice (**Figure**

3f). The structure of all the perovskites is retained after a high temperature reducing treatment in 5%H_2/95% N_2 at 1050 ^{o}C, for 20 h, illustrating a good structural redox-stability.

H_2-temperature-programmed-reduction (H_2-TPR) profiles of the as-prepared LSCM$_A$- and LSCMRu$_{A-5}$ oxides are given in **Figure 3g**. A broad reduction band at 529 ^{o}C is observed in the H_2-TPR plot of as-prepared LSCMRu$_{A-x}$ (x=0) and the reduction band could be ascribed to the reduction of Cr and Mn ions at B-site. The reduction band shifts to a higher temperature (588 ^{o}C) for reduced LSCMRu$_{A-0}$, which was undergoing calcination at reducing atmosphere. This illustrates that hydrogen is still consumed even that the LSCMRu$_{A-5}$ oxide was heated in the reducing atmosphere for the long term. The addition of Ru in LSCMRu$_{A-5}$ oxide significantly lowers the reduction temperatures. The intensity of reduction band increases and the band temperature shifts to lower values (282~409 ^{o}C) for LSCMRu$_{A-5}$. The decrease of the reduction temperature is clearly due to the high hydrogen dissociation activity.[17] In the present case, numerous Ru nanoparticles were exsolved in the process of H_2-TPR measurement. We can also deduce that the starting exsolved temperature of Ru nanoparticles is about 282 ^{o}C in pure H_2. This reveals that the reducing process in lower temperatures (<500 ^{o}C) is sufficient for the exsolved Ru nanoparticles on the surface of LSCMRu$_{A-5}$ in pure H_2. This result was confirmed by an additional STEM-EDS analysis (Supporting Information, Figure S7). Moreover, a strong reduction peak is observed and it shifts toward lower temperature further (332.6 ^{o}C) in reduced LSCMRu$_{A-5}$. This sharp reduction peak is ascribed to the additional metallic Ru nanoparticles exsolved from in the lattice.

The electrochemical impedance spectra (EIS) of LSCMRu$_{A-5}$ electrodes were measured with a SSZ (10% Sc$_2$O$_3$-stabilized-ZrO$_2$) supported half symmetric cell configuration LSCMRu$_{A-5}$-SSZ|SSZ|LSCMRu$_{A-5}$-SSZ in wet 5% H$_2$/N$_2$ under open voltage conditions. The ohmic resistances are normalized to zero to obtain the detailed information between impedance arcs at various temperatures (Supporting Information, Figure S8). It can be seen that the resistance polarization (R$_p$) of the LSCMRu$_{A-x}$ electrodes decrease with the increase of Ru-content both in air and wet 5%H$_2$/N$_2$, illustrating a facilitated ORR and HOR processes in electrode reaction simultaneously. The apparent activation energies (E$_a$) for R$_p$ were calculated and reveals that E$_a$ of LSCMRu$_{A-x}$ become lower when the content of Ru increase in both air and 5% H$_2$/N$_2$ conditions. This implies that ORR and HOR of Ru-doping electrode materials are faster than those of pure electrode both in air and wet 5%H$_2$/N$_2$, respectively. The enhanced ORR performance of reduced LSCMRu$_{A-5}$ due to the formation of Ru/RuO$_2$ nanoparticles was further studied via the evolution of impedance with the various oxygen partial pressure (pO$_2$). As showed in **Figure 4a** and **4b**, the R$_p$ of as-prepared and reduced LSCMRu$_{A-5}$ at various pO$_2$ were lower than those of reduced sample. For instance, the minimum R$_p$ of 0.11 Ω cm^{-2} was present for the reduced LSCMRu$_{A-5}$ electrode in pure oxygen at 750 ^{o}C, while the as-prepared LSCMRu$_{A-5}$ electrode shows the R$_p$ value of 0.15 Ω cm^{-2} at the same condition. This phenomenon illustrates that R$_p$ was reduced by 27% as the Ru/RuO$_2$ formed on the surface of LSCMRu$_{A-5}$. The lower *n* values calculated from $R_p = k(pO_2)^{-n}$, suggest that the formation of RuO$_2$ is a significant benefit for the ORR process in the reduced LSCMRu$_{A-5}$ electrode.[18]

The oxygen desorption properties of the as-prepared LSCMRu$_{A-0}$ and LSCMRu$_{A-5}$ oxides were studied through an oxygen temperature-programed desorption (O$_2$-TPD) technique under argon from 100 to 900 ^oC (Supporting Information, Figure S9). In this case, a lot of oxygen vacancies formed and a phase transition in reduced LSCMRu$_{A-0}$ caused a transformation from an oxygen vacancy disordered structure (*R-3c*) to an ordered structure (*Pm-3m*).[19] Interestingly, the Ru-doped oxide LSCMRu$_{A-5}$ shows two distinguish desorption peaks at 395 ^oC and 550 ^oC respectively and a strong β-oxygen desorption peak clearly occurred. This feature could be due to the partial reduction of the transition metal in the B-site after the presence of Ru, leading to a larger oxygen vacancy concentration. However, only a broad band of oxygen desorption is observed in reduced LSCMRu$_{A-5}$ powders, meaning a strong interaction between oxygen and exsolved Ru/RuO$_2$ nanoparticles at the temperature ranging from 400 to 900 ^oC.

Figure 4c illustrates the R$_p$ as function of pH$_2$ for LSCMRu$_{A-5}$-SSZ symmetrical electrodes at 750 ^oC. The resistance decreased significantly with the increase of pH$_2$. The lowest R$_p$ value of 0.41 Ω cm^{-2} was obtained as the pH$_2$ was 97% H$_2$. Furthermore, the various of log R$_p$ vs log pH$_2$ showed a linear dependent behavior at 750 ^oC, which reavels that the exsolved Ru nanoparticles in stronger reducing atmosphrere could enhance HOR more greatly. **Figure 4d** dipictes the AC impedance spectra of half cell with LSCMRu$_{A-5}$ symmetrical electrodes at 750 ^oC under different applied potentials to study the change of R$_p$ in SOEC mode. In order to exsolve the Ru/RuO$_2$ nanoparticles in LSCMRu$_{A-5}$, the reduced and re-oxdied powders were obtained after a pre-calcination. The R$_p$ of the cell based on LSCMRu$_{A-5}$ symmetrical electrodes are improved with the increase of applied

voltages in 50% absolute humidity (AH). The decreasing of the R_p is ascribed to the enhanced electrode activation under external voltages, which is still lower than the reported value for steam electrolysis with LSCM cathode in previous works.[20]

To characterize the utility and multifunctional electrochemical performance of the LSCMRu$_{A-5}$-SSZ composite electrode materials in practical symmetric cells, we used electrolyte-supported cells based on a SSZ electrolyte with the symmetric configuration of LSCMRu$_{A-5}$-SSZ/SSZ/LSCMRu$_{A-5}$-SSZ (x=0.05) (Supporting Information, Figure S10). To obtain higher cell performance, the cell was heated at 750 °C in 5% H_2/N_2 for 20 h to modify the microstructure of both fuel electrode and oxygen electrode simultaneously through in-situ growth Ru nanoparticles. The single-cell performance was showed in **Figure 5** and the same cell was operated in 50% H_2O/H_2 for EC, 3% H_2O/H_2 for FC, and 50% H_2O/H_2 for reversible cell (RC) at temperatures between 650 and 750 °C, respectively. In EC mode, the current densities were the range from -0. 5 A cm^{-2} to -1.75 A cm^{-2} at 650~750 °C, respectively (**Figure 5a**). These values are higher than those without Ru-doping electrode in an LSCMRu$_{A-5}$-SSZ/SSZ/LSCMRu$_{A-5}$-SSZ cell tested at the same conditions (Supporting Information, Figure S11). Since the cell was tested in FC mode, it demonstrated a maximum power density of 0.55 W cm^{-2} at 750 °C as pure hydrogen as a fuel (**Figure 5b**). The performance depicts in this work is comparable to those reported recently for symmetric solid oxide fuel cells (Supporting Information, Table S7). As there are numerous Ru nanoparticles on the surface of electrode, it seems that the reduced LSCMRu$_{A-5}$ electrode illustrates high electrocatalytic activity toward HOR for fuel electrode and ORR for oxygen electrode respectively. It is reported that the optimal

condition for oxygen electrode catalytically active for both the ORR and the OER is not only a mixed-valent or metallic oxide at its equilibrium oxidation state at the pO_2 and operating temperature of the cell, but also a catalytic electrode with a high concentration of oxygen vacancies.[21] In our case, the superior ORR activity presents here due to a mixed-valent perovskite oxide LSCMRu$_{A-5}$ exhibits various oxidation states for Mn and Ru, as well as metallic oxide RuO_2 formed via in-situ growth on the surface of perovskite. Moreover, the LSCMRu$_{A-5}$ symmetric electrode also delivers stable performance switching between EC and FC at 750 ^oC under a constant current density，for example, -0.2 A cm^{-2} for EC and 0.2 A cm^{-2} for FC respectively (**Figure 5c**). In RC mode, the device showed excellent reversible electrochemical performance with the current density as -0.56/+0.33 A cm^{-2} under 1.3V/0.8V at 750 ^oC. The device performance is much higher than that of the recently reported symmetric cell LSCM/YSZ/LSCM (around -0.31/+0.28 A cm^{-2} under 1.3V/0.8V at 900 ^oC)[7b].However, it is still of importance to reduce the thickness of electrolyte to make a lower ohmic resistance or optimize the morphology of cell to raise the efficiency, which could have a significant increase of the cell performance. Although a small degradation of performance occurred after a 10-cyclic EC/FC test, the cell still demonstrates good long-term stability at intermediate temperatures (**Figure 5d**). This slight degradation could be ascribed to the partial exfoliated-RuO_2 nanoparticles from the LSCMRu$_{A-5}$ substrates. From the HRTEM image after the tests (**Figure 6**), an uniform crater-like pit is observed in the surface of LSCMRu$_{A-x}$ perovskite, where we can achieve the lattice fringes at a spacing of 0.563 nm for the (104) plane of LSCMRu$_{A-5}$ lattice.

3. Conclusions

In summary, we demonstrate a novel symmetric electrode via Ru substitution into A-site deficient LSCMRu$_{A-x}$ (x=0-0.05) to form a highly active nanostructure due to the exsolved Ru nanoparticles in reducing atmosphere. We found that good dispersion of the nanoparticles on LSCMRu$_{A-5}$ not only enhanced fuel oxidation reaction greatly but also benefited for the H_2O electrolysis simultaneously. Interestingly, the core-shell structured Ru/RuO$_2$ nanoparticles could also be formed on LSCMRu$_{A-x}$ surface in an oxidation atmosphere and they greatly improved the ORR and OER activity of oxygen electrodes. Our study demonstrated a simple method to fabricate the highly active nanostructures of both fuel electrode and oxygen electrode simultaneously for single reversible SSOCs. Although the peak power densities of our cells are not superior high in SOFC mode, which is due to the thick electrolyte and lower electrical conductivity of LSCM, our work still provides insights that Ru/RuO$_2$-supported perovskites as heterostructured catalysts prepared by *in-situ* growth method could be promising novel catalysts for the issue of fuel consumption and fuel alternatives.

4. Experimental

The (La$_{0.75}$Sr$_{0.25}$)$_{0.9}$Cr$_{0.5}$Mn$_{0.5-x}$Ru$_x$O$_{3-\delta}$ (x=0, 0.25, and 0.05) (denoted as LSCMRu$_{A-x}$ (x=0-0.05)) were prepared by solid-state reaction method performed in air. Stoichiometric amounts of pre-dried purity of the La$_2$O$_3$ (99.99%), SrCO$_3$ (99.99%), Cr$_2$O$_3$ (99.99%), MnCO$_3$ (AR) and RuO$_2$ (AR) were mixed and ball milled for 1h with the amount of ethanol. The mixture powder was then calcined in air at 1400 °C for 10h. On a reduced sample, the as-prepared powders were first reduced in 5% H$_2$/N$_2$ at 800 °C for 20 h. Then, the reduced powders were oxidized again in air at 800 °C for 3 h and the re-oxidized sample was

obtained finally. The pellets of Sc_2O_3-stabilized-ZrO_2 (($Sc_2O_3)_{0.1}(CeO_2)_{0.01}(ZrO_2)_{0.89}$, SSZ) electrolyte was purchased from Ningbo SOFCMAN Energy Technology Co., Ltd.

The reaction products and stability in reduction atmosphere were characterized by X-ray diffraction (XRD) for phase identification and to assess phase purity. The phase characterization was performed with powder X-ray diffraction (XRD, Bruker D2 PHASER, Germany) operated at 30 kV and 10 mA using Cu K_α radiation with a wavelength of 1.54 Å at room temperature. The scans were measured in the 2θ rang of 10-90° at a rate of 0.02 °/s. Rietveld refinements on XRD patterns were calculated with Reflex module in Materials Studio 5.5. HT-XRD measurements from room temperature to 1000 °C in air were carried out on a Bruker D8 ADVANCE X-ray diffraction over a 2θ ranging from 20° to 80° with a step size of 0.01 °/s. mm. HR-TEM and STEM-EDS analysis were inspected on a JEM-F200 machine. The fractured cross-section of fuel cells was carried out on GeminiSEM 500. X-ray photoelectron spectroscopy (XPS, Thermo Scientific K-Alpha, USA) was characterized to analyze the oxidation states and relative abundance of the elements at the surface of nanoparticles. The binding energies (BEs) of elements in samples were analyzed by the CasaXPS software. Raman spectra were recorded with Raman spectrometer (InViaReflex, Renishaw, UK). The wavelength of the excitation laser was 632.8 nm from a He-Ne laser.

Temperature programmed reduction with hydrogen (H_2-TPR, Autochem II 2920, Micromeritics, USA) was used to characterize the reducibility of the materials. Samples of 100 mg were first pre-treated in Ar atmosphere for 1h at 300 °C with a 50 mL (STP) min^{-1} flow by a ramp of 10 °C min^{-1}, and then cooling down to 30 °C.after cooling down, heating

the reactor up to 900 °C, at 10 °C min^{-1} in a 50 mL min^{-1} flow consisted of 5 mol% H$_2$ in Ar

balance, while collecting the equipment output signal. The H$_2$ consumption and the

percentage of reduction were monitored using an in-situ thermal conductivity detector

(TCD). Temperature programmed desorption of oxygen (O$_2$-TPD) experiments were

carried out on Autochem II 2920. Samples of 100 mg were degassed in Ar atmosphere

during 1h, in a 50 mL (STP) min^{-1} flow at 300 °C, then cooling down to 30 °C. Oxygen

adsorption was carried out by exposing the samples to a flow of 10 mol% O$_2$ in Ar at 30 °C.

Afterward, the reactor was purged with a 50 mL min^{-1} Ar flow during 90 min to remove O$_2$.

Finally, the reactor was heated up to 900 °C in Ar by using a linear temperature program

at a ramping rate of 10 °C min^{-1}.

The electrode for impedance tests was fabricated as follows: The mixed slurry was

made of pure LSCMRu$_{A-x}$ (x=0-0.05) powders with organic additive containing 95 wt%

terpineol and 5 wt% turpentine. The mixture was then screen-printed onto both sides of

SSZ electrolyte followed by calcination at 1000 °C for 4 h. Then the electrode was covered

with silver paste and silver wires as current collectors. The electrochemical performances

of the electrode under air and wet 5% H$_2$\95%N$_2$ were investigated by electrochemical

impedance spectroscopy (EIS) using the work station (Solartron Analytical SI 1260 &

1287, UK) with a frequency range of 0.01 Hz to 1 MHz between 600 °C and 750 °C. The

raw data was analyzed by the Zview software to fit the obtained results. The polarization

resistance (R_p) is deriving from the real intercepts between high frequencies and low

frequencies by the spectra.

For single-cell tests, a cell with a configuration of

LSCMRu$_{A-5}$-SSZ|SSZ|LSCMRu$_{A-5}$-SSZ was fabricated. The mixed electrode materials of LSCMRu$_{A-5}$ and SSZ powders (with a mass ratio of 7:3) were ball-milled in ethanol for 10 h, followed by an additional ball-milling with organic additive containing 95 wt% terpineol and 5 wt% turpentine for 2 h. Then, the suspension was screen-printed onto both sides of SSZ electrolyte and dried in an oven at 90 °C. Finally, the cell was heated in air at 1000 °C for 4 h. The active area of both sides of the cell is about 0.20 cm^2. The silver paste and silver wires were used as current collectors. The output performance of the single cell in FC mode was performed in air and humidified H$_2$ used as the oxidant and fuels, respectively. Meanwhile, 50% H$_2$O steam was fed as inlet gas to the one side of LSCMRu$_{A-5}$ electrode in EC mode. Current-voltage (*I-V)* plots of RSOCs were measured in a two-electrode and performed linear sweep voltammetry both in FC mode and EC mode, respectively.

Supporting Information

Supporting Information is available from the Wiley Online Library or from the author.

Conflict of Interest

The authors declare no competing financial interest.

Keywords:

Perovskite oxide, core-shell particles, exsolution, SOCs, electrochemical activity

References

[1] a) B. Dunn, H. Kamath, J.-M. Tarascon, *Science (New York, N.Y.)* **2011**, 334, 928; b) R. Braun, S. Jensen, C. Graves, M. Mogensen, C. Wendel, S. Barnett, Z. Gao, *Energy Environ. Sci.* **2015**, 8; c) Z. Yi, H. Yongxiu, G. Sifan, L. Lin, *AIP Conference Proceedings* **2018**, DOI: https://doi.org/10.1063/1.5030311020007; d) E. Wachsman, C. Marlowe, K. Lee, *Energy Environ. Sci.* **2012**, 5, 5498.

[2] a) M. J, P. O, *Fuel Cells* **2017**, 17, 7; b) Y. Luo, Y. X. Shi, Y. Zheng, N. S. Cai, *Journal of Power Sources* **2017**, 340, 60; c) J.-H. Myung, D. Neagu, D. N. Miller, J. T. S. Irvine, *Nature* **2016**, 537, 528; d) J. T. S. Irvine, D. Neagu, M. C. Verbraeken, C. Chatzichristodoulou, C. Graves, M. B. Mogensen, *Nat. Energy* **2016**, 1, 15014.

[3] a) B. C. H. Steele, A. Heinzel, *Nature* **2001**, 414, 345; b) D. J. L. Brett, A. Atkinson, N. P. Brandon, S. J. Skinner, *Chem. Soc. Rev.* **2008**, 37, 1568.

[4] a) A. Aguadero, D. Perez-Coll, J. A. Alonso, S. J. Skinner, J. Kilner, *Chemistry of Materials - CHEM MATER* **2012**, 24, 2655; b) A. V. Virkar, *Int. J. Hydrogen Energy* **2010**, 35, 9527; c) M. M. Kuklja, E. A. Kotomin, R. Merkle, Y. A. Mastrikov, J. Maier, *Phys Chem Chem Phys* **2013**, 15, 5443; d) Y. Chen, W. Jung, Z. Cai, J. Kim, T. Harry, B. Yildiz, *Energy Environ. Sci.* **2012**, 5, 7979; e) S. Sengodan, S. Choi, A. Jun, T. Shin, Y.-W. Ju, H. Y. Jeong, J. Shin, J. Irvine, G. Kim, *Nat. Mater.* **2014**, 14.

[5] C. Graves, S. D. Ebbesen, S. H. Jensen, S. B. Simonsen, M. B. Mogensen, *Nat Mater* **2015**, 14, 239.

[6] J. Druce, H. Téllez Lozano, M. Burriel, M. Sharp, L. Fawcett, S. Cook, D. McPhail, T. Ishihara, H. Brongersma, J. Kilner, *Energy Environ. Sci.* **2014**, 7.

[7] a) J. C. Ruiz-Morales, D. Marrero-López, J. Canales-Vázquez, J. T. S. Irvine, *RSC Advances* **2011**, 1, 1403; b) D. M. Bastidas, S. Tao, J. T. S. Irvine, *J. Mater. Chem.* **2006**, 16, 1603; c) C. Su, W. Wang, M. L. Liu, M. O. Tade, Z. P. Shao, *Advanced Energy Materials* **2015**, 5, n/a.

[8] Q. Liu, X. Dong, G. Xiao, F. Zhao, F. Chen, *Advanced Materials* **2010**, 22, 5478.

[9] a) J. C. Ruiz-Morales, H. Lincke, D. Marrero-López, J. Canales-Vázquez, P. Núñez, *Bol. Soc. Esp. Ceram. Vidrio* **2007**, 46, 218; b) J. Peña-Martínez, D. Marrero-López, D. Pérez-Coll, J. C. Ruiz-Morales, P. Núñez, *Electrochim. Acta* **2007**, 52, 2950; c) J. Canales-Vázquez, J. C. Ruiz-Morales, D. Marrero-López, J. Peña-Martínez, P. Núñez, P. Gómez-Romero, *J. Power Sources* **2007**, 171, 552; d) Y. Song, Q. Zhong, W. Tan, C. Pan, *Electrochim. Acta* **2014**, 139, 13; e) L. dos Santos-Gómez, J. M. Compana, S. Bruque, E. R. Losilla, D. Marrero-López, *J. Power Sources* **2015**, 279, 419; f) J. Zhou, G. Chen, K. Wu, Y. Cheng, *Journal of Power Sources* **2014**, 270, 418; g) H. Qi, T. Thomas, W. Li, W. Li, F. Xia, N. Zhang, E. M. Sabolsky, J. Zondlo, R. Hart, X. Liu, *ACS Applied Energy Materials* **2019**, 2, 4244; h) A. B. Munoz-Garcia, D. E. Bugaris, M. Pavone, J. P. Hodges, A. Huq, F. Chen, H. C. zur Loye, E. A. Carter, *J Am Chem Soc* **2012**, 134, 6826.

[10] a) J. T. S. Irvine, P. Connor, **2014**; b) W. Chueh, Y. Hao, W. Jung, S. Haile, *Nat. Mater.* **2011**, 11, 155.

[11] a) G. Corre, G. Kim, M. Cassidy, J. Vohs, R. Gorte, J. Irvine, *Chemistry of Materials - CHEM MATER* **2009**, 21; b) J. M. Vohs, R. J. Gorte, *Advanced Materials* **2009**, 21, 943; c) D. Ding, X. Li, S. Y. Lai, K. Gerdes, M. Liu, *Energy & Environmental Science* **2014**, 7, 552.

[12] a) D. Neagu, G. Tsekouras, D. N. Miller, H. Ménard, J. T. S. Irvine, *Nat. Chem.* **2013**, 5, 916;

b) D. Neagu, T.-S. Oh, D. N. Miller, H. Ménard, S. M. Bukhari, S. R. Gamble, R. J. Gorte, J. M. Vohs, J. T. S. Irvine, *Nature Communications* **2015**, 6, 8120; c) D. Neagu, E. Papaioannou, W. K. B. Wan Ramli, D. Miller, B. Murdoch, H. Menard, A. Umar, A. Barlow, P. Cumpson, J. Irvine, I. Metcalfe, *Nat. Commun.* **2017**, 8; d) O. Kwon, S. Sengodan, K. Kim, G. Kim, H. Y. Jeong, J. Shin, Y.-W. Ju, J. W. Han, G. Kim, *Nat. Commun.* **2017**, 8, 15967; e) B. Hua, N. Yan, M. Li, Y.-F. Sun, Y. Zhang, J. Li, T. Etsell, P. Sarkar, J.-L. Luo, *Adv. Mater.* **2016**, 28; f) C. Duan, R. Kee, H. Zhu, C. Karakaya, Y. Chen, S. Ricote, A. Jarry, E. Crumlin, D. Hook, R. Braun, N. Sullivan, R. O'Hayre, *Nature* **2018**, 557; g) N. Hou, T. Yao, P. Li, X. Yao, T. Gan, L. Fan, J. Wang, X. Zhi, Y. Zhao, Y. Li, *ACS Applied Materials & Interfaces* **2019**, 11, 6995.

[13] J. Goodenough, P. Raccah, *Journal of Applied Physics - J APPL PHYS* **1965**, 36, 1031.

[14] S. Tao, J. T. S. Irvine, *Chem Mater* **2006**, 18, 5453.

[15] C. Howard, H. Stokes, *Acta Crystallographica Section B-structural Science - ACTA CRYSTALLOGR B-STRUCT SCI* **1998**, 54, 782.

[16] E. Paoli, F. Masini, R. Frydendal, D. Deiana, C. Schlaup, M. Malizia, T. Hansen, S. Horch, I. Stephens, I. Chorkendorff, *Chem. Sci.* **2014**, 6.

[17] A. Yan, B. Liu, B. Tu, Y. Dong, M. Cheng, S. Song, P. Tsiakaras, *Journal of Fuel Cell Science and Technology - J FUEL CELL SCI TECHNOL* **2007**, 4.

[18] F. Mauvy, J. Bassat, E. Boehm-Courjault, J. P. Manaud, P. Dordor, J. Grenier, *Solid State Ionics* **2003**, 158, 17.

[19] S. McIntosh, J. Vente, W. Haije, D. Blank, H. Bouwmeester, *Chemistry of Materials - CHEM MATER* **2006**, 18, 2187.

[20] S. Chen, K. Xie, D. Dong, H. Li, Q. Qin, Y. Zhang, Y. Wu, *Journal of Power Sources* **2015**, 274, 718.

[21] a) J. Suntivich, K. J. May, H. A. Gasteiger, J. B. Goodenough, Y. Shao-Horn, *Science* **2011**, 334, 1383; b) B. Zhao, L. Zhang, D. Zhen, S. Yoo, Y. Ding, D. Chen, Y. Chen, Q. Zhang, B. Doyle, X. Xiong, M. Liu, *Nat. Commun.* **2017**, 8, 14586; c) N. Tsvetkov, Q. Lu, L. Sun, E. J. Crumlin, B. Yildiz, *Nat. Mater.* **2016**, 15, 1010; d) D. N. Mueller, M. L. Machala, H. Bluhm, W. C. Chueh, *Nat. Commun.* **2015**, 6, 6097; e) Y.-L. Lee, J. Kleis, J. Rossmeisl, Y. Shao-Horn, D. Morgan, *Energy Environ. Sci.* **2011**, 4, 3966.
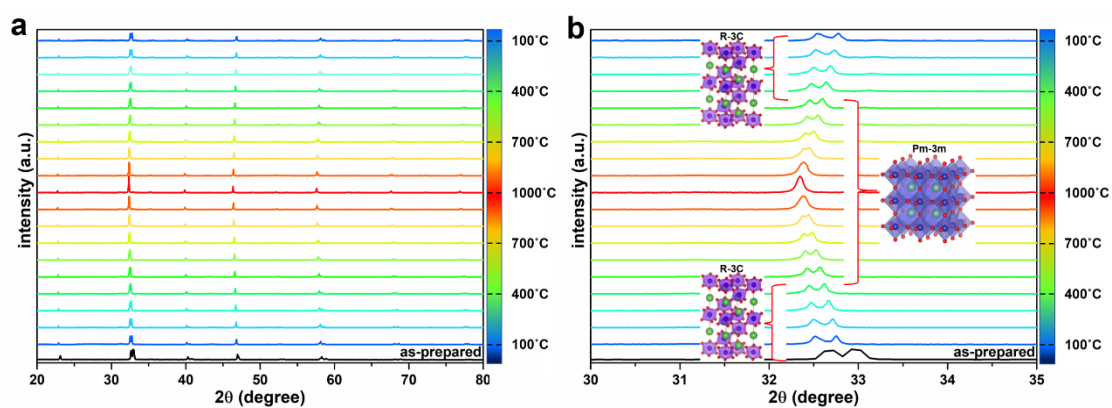
Figures:

Figure 1. The evolution of crystal structure of LSCMRu$_{A-x}$ (x=0.05) in air at high temperatures. a) HT-XRD pattern of as-prepared sample which was tested in air in a heating-cooling cycle in the temperature range of RT to 1000 °C. b) Local HT-XRD patterns (30°-35°) of as-prepared sample in a). LSCMRu$_{A-x}$ (x=0.05) clearly shows a *R-3c* space group at low temperature. The *Pm-3m* space group was observed at higher temperature and *R-3c* space group is dominant again when temperature decreases.

Figure 2. The morphology of exsolved Ru nanoparticles on the surface of reduced LSCMRu$_{A-5}$ powders.

a) HR-TEM image of reduced sample; and b) magnified HR-TEM image of Ru nanoparticle. c) STEM image of the reduced LSCMRu$_{A-5}$ with the EDS elemental mapping images of La, Sr, Cr, Mn, Ru, and O, respectively.
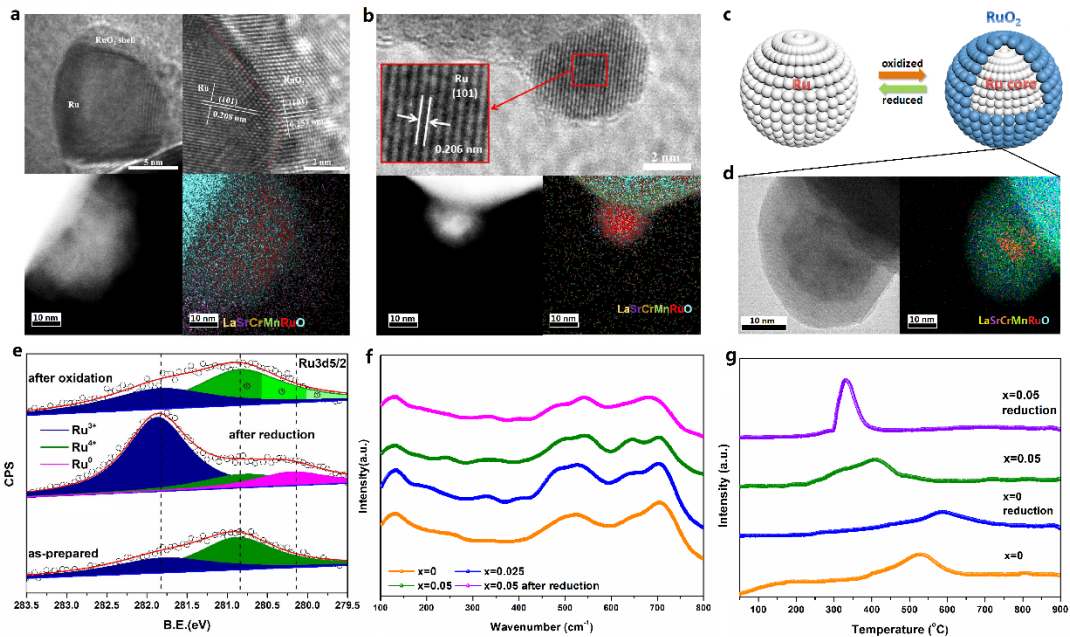
Figure 3. *In-situ* growth of Ru/RuO$_2$ core-shell nanoparticles. a) HR-TEM image, magnified HR-TEM image and STEM-EDS mapping images of a Ru/RuO$_2$ core-shell nanoparticle, which was oxidized at 750 °C in air for 2 h from a Ru nanoparticle. b) HR-TEM and STEM-EDS mapping images of a Ru nanoparticle, which was reduced at 750 °C in 5% H$_2$/N$_2$ for 2 h from a Ru/RuO$_2$ core-shell nanoparticle. c) The schematic of transformation between Ru and Ru/RuO$_2$ core-shell particle. d) TEM and EDS mapping images of a Ru/RuO$_2$ core-shell nanoparticle which was oxidized in air at 500 °C for 3 h from the reduced LSCMRu$_{A-5}$ sample. e) XPS spectra of Ru treated in different conditions. f) Raman spectra and g) H$_2$-TPR curves of LSCMRu$_{A-x}$ (x=0 and 0.05). Both as-prepared samples and reduced samples were studied. The reduced samples were prepared through a heating process at 750 °C in 5% H$_2$/N$_2$ for 20 h from as-prepared powders.
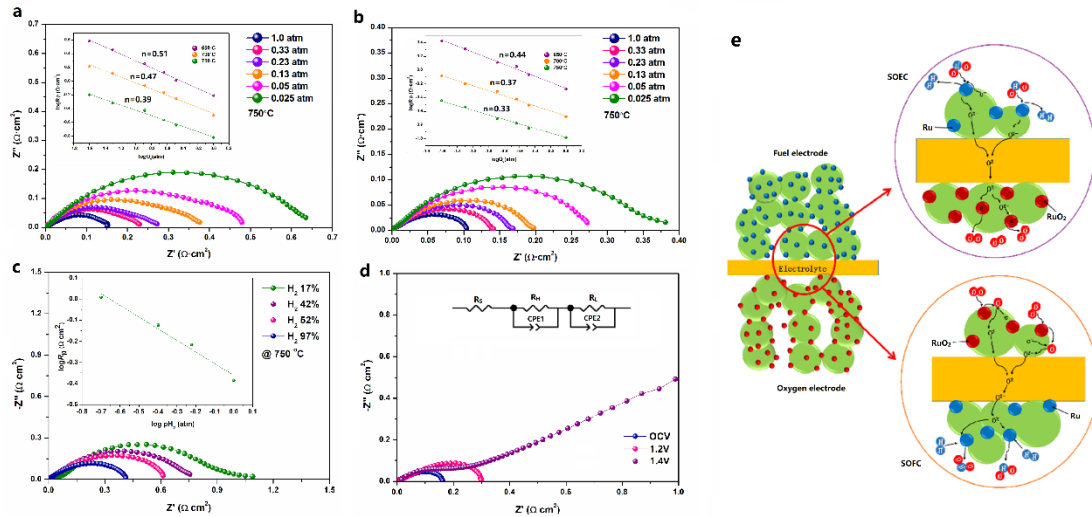
Figure 4. Impedance spectra of as-prepared LSCMRu$_{A-5}$ a) and reduced LSCMRu$_{A-5}$ b) electrodes as a function of pO$_2$ at 750 °C. c) The resistance versus hydrogen partial pressure for LSCMRu$_{A-5}$ at 750 °C. d) AC impedance spectra of the cell with LSCMRu$_{A-5}$ as symmetrical electrodes under open-circuit condition and DC potentials of 1.2 and 1.4 V at 750 °C in 50% AH. e) The schematic of electrocatalytic reaction mechanisms in FC and EC modes respectively. The insets are: the evolution of *n* values between R$_p$ and pO$_2$ on as-prepared LSCMRu$_{A-5}$ and reduced LSCMRu$_{A-5}$ in a) and b).
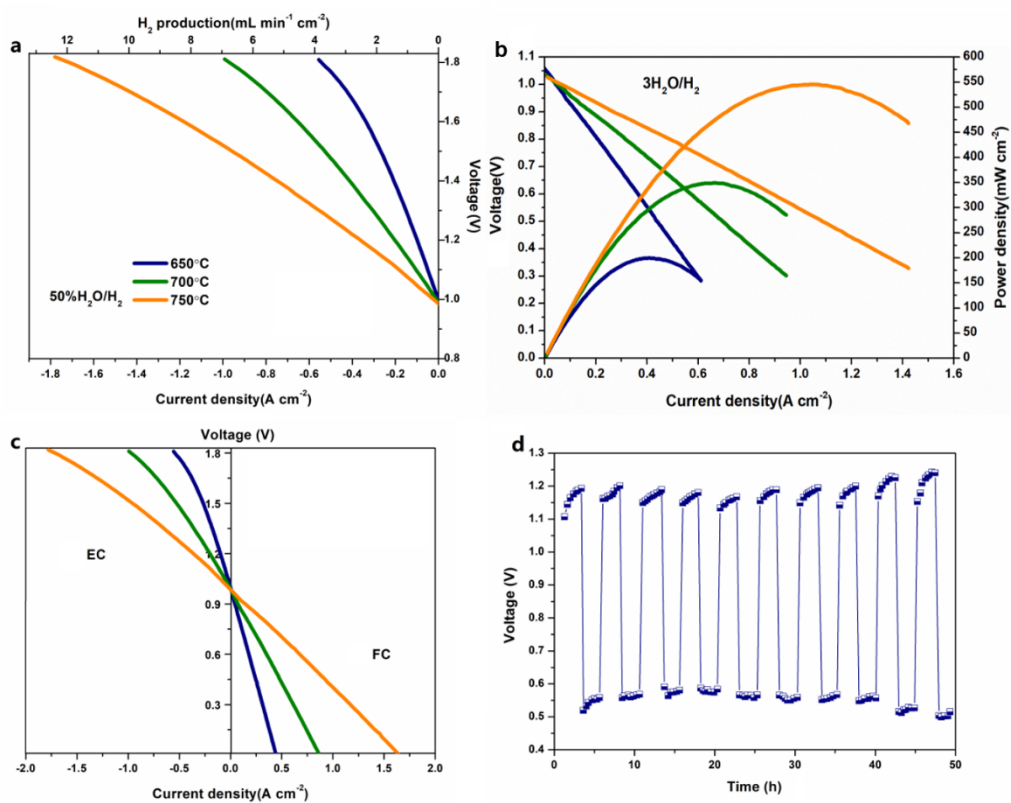
Figure 5. Cell performance and durability at different modes. a), H_2 production in EC mode at various temperatures under 50% H_2O/N_2. b), Power densities in FC mode at various temperatures in 3% H_2O/H_2. c), The reversible performance between FC and EC modes in 50 % H_2O/H_2. d), 10-cyclic EC/FC test was conducted at 800 °C in 50% H_2O/H_2 at +0.3/-0.3 A cm^{-2}.
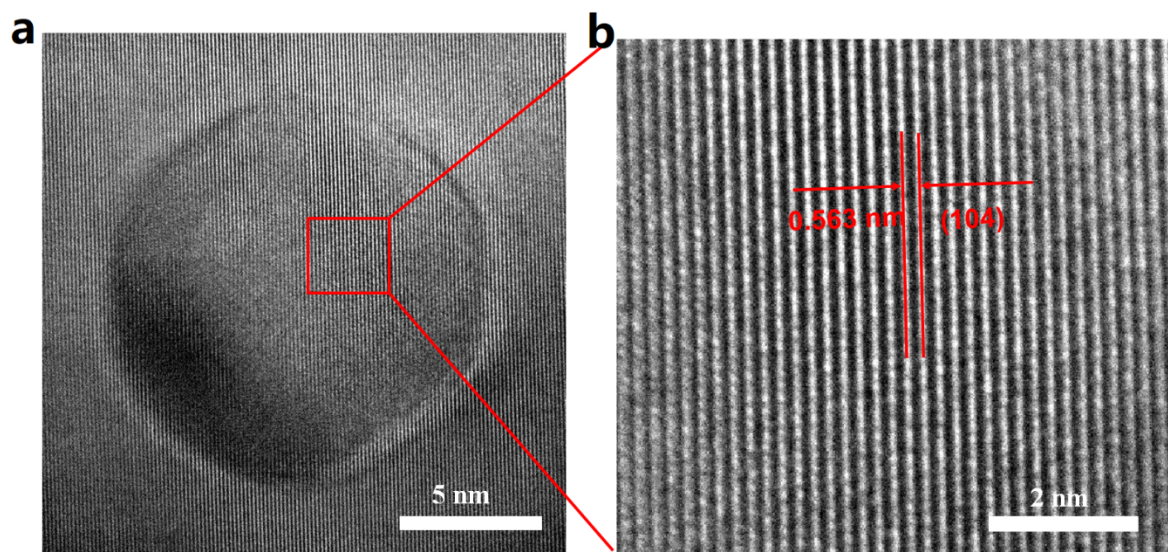
Figure 6. HRTEM of images of LSCMRu$_{A-5}$ after a 10-cyclic EC/FC test. A crater-like pit was observed in

LSCMRu$_{A-5}$ powders after the tests.

Graphical abstract: